Hemodynamics Model Illustrating Transradial Delivery of Anti-Tau Nanoparticle For Prodromal Alzheimer's Disease Intervention

Michael Khalfin

Abstract

Alzheimer's Disease is an extremely prevalent neurodegenerative disease with over six million cases in the US. This disease causes progressive cognitive decline via tau pathology, which is a consequence of misfolded proteins. It starts in the locus coeruleus, proceeding to the transentorhinal cortex, then to other limbic and cortical areas. Current FDA-approved medications such as memantine, donepezil, and aducanamab are ineffective at halting degeneration. Understanding how mechanistically we need to treat tau pathology will generate more effective therapeutics and was the basis of a tau propagation model that investigated therapeutic efficacy based on neuronal survival rate. However, since there was no method for administering the treatment, the premise behind this project was embedding such therapeutics in biodegradable nanoparticles that could travel through arteries and reach the transentorhinal cortex. A hemodynamic model was created based on the Hagen–Poiseuille and Bernoulli equations to find the arterial velocity in blood flow and simulate the attachment of nanomotors. The results identified time for arterial travel and minimum amount and speed of nanomotors. A statistical test indicated that using at least 18 mm of nanomotors is beneficial for a lower total time. The *in silico* model was validated through comparison with average *in vivo* values for arterial blood velocity, which revealed that the model had physical limitations, but was still suggestive of major trends. The results favorably portrayed the nanoparticle's biological realism, making it a suitable candidate for potentially reversing Alzheimer's Disease with negligible invasiveness.

Table of Contents

Abbreviations

Aβ - amyloid-beta

AD - Alzheimer's Disease

LC - locus coeruleus

MAP - microtubule associated protein

NFTs - neurofibrillary tangles

NP - nanoparticle

TEC - transentorhinal cortex

1. Introduction

Dementia refers to the significant decline in memory, cognition, awareness, language, and decision-making. Individuals with dementia often have difficulty partaking in activities of daily living, while also experiencing physical ailments such as weight loss and nutritional deficiency since they struggle with self-care[1]. Additionally, there are other psychological and social tolls on individuals with dementia and their loved ones. The burden of care falls on children or partners, which requires a considerable amount of time and sacrifice[2]. Individuals may express distress, irritability and even outbursts of anger directed towards their caregivers, causing emotional turmoil for those involved[2]. A flat affect, or the inability to show feeling[3], can be equally catastrophic because of the frustration resulting from mental numbness. Moreover, assistance and rehabilitation programs are overwhelmingly expensive, so families impacted by dementia may become subject to a large financial burden of more than $200,000 over 7 years[4]. Thus, the need to address dementia is greater than just a scientific requisite.

Alzheimer's Disease (AD) is a neurodegenerative disorder that is the leading cause of dementia among older individuals[5]. Unfortunately, while researchers have made great strides in elucidating hallmark pathologies in AD, there is still no cure. Creating effective treatments for this illness has become increasingly important, as by the middle of the 21st century, 13.8 million Americans are projected to suffer from AD[5]. Successfully combating AD must involve a comprehensive understanding of disease pathology and the employment of modern resources in a novel way.

A. Tau Pathology

One of the fundamental causes of AD is the accumulation of aberrant, or mutated, tau proteins.* Tau belongs to a class of important proteins known as major microtubule associated proteins (MAP). In healthy tau-expressing neurons, tau functions in maintaining the cell's architecture. Specifically, tau helps build and maintain the structure of the neuronal cell body, called the cytoskeleton. It interacts with other MAPs including MAP1 and MAP2 to assist in this function[9]. Secondly, the tau protein is involved in synaptic plasticity, which is the neuron's ability to form structural connections with other neurons[10]. These connections are highly important for cognitive functions, such as learning and memory. When tau is mutated, the aberrant conformation of the protein wreaks havoc, and induces mechanisms that will destroy neurons, leading to gradual brain degeneration.

The reason why mutated tau is so harmful compared to the wild-type, or normal, conformation of tau is because of the change in the mutated protein's folding patterns. To elaborate, proteins undertake highly specific shapes, folding patterns, and amino acid compositions to carry out functions that are compatible with their role in the cellular environment. Therefore, when tau is misfolded, the abnormal conformation disables the protein from carrying out its normal functions. One biochemical basis of this

* There are other major causes of AD including amyloid-beta pathology[6] (discussed later), impairment of microglia and astrocytes[7], dysfunctional acetylcholine (AcH)[8]. All these compounding factors are influential in the progression of AD.

transformation is hyperphosphorylation, or the saturation of at least 45 phosphate binding sites on the tau protein's exterior[11]. This is 3-4 times the normal amount, and as a result, tau becomes vulnerable to clustering, leading to the formation of neurofibrillary tangles (NFT)[9]. The structure of such tangles is a mix of paired helical filaments with single filaments[9]. NFTs are inert due to their chemical composition. Although NFTs are chemically inactive, they are extremely problematic because they replace healthy tau proteins and aggregate in otherwise healthy neurons, eventually causing neuronal cell death[12]. Furthermore, they spread between neurons in a molecular process referred to as tau propagation.

B. Tau Propagation

While there are a few key pathologies that are responsible for AD onset, the present study mainly focuses on tau since its root location in the brain is known[13]. It is transferred between neurons, bolstering the brainwide progression of AD and brain degeneration. Recent research has enhanced our understanding of the complex mechanism of tau propagation[13,14,15,16,17].

Braak Stages	Duration	Impacted Region
I, II (Early)	Years-decades	Locus coeruleus (LC) and transentorhinal cortex (TEC)[13]
III, IV (Middle)	Years	Proper entorhinal cortex, Ammon's horn sector[13]
V, VI (Late)	Years	All neocortical areas[13]

Table 1: Spread of tau on a macroscopic level, based on the Braak stages

The Braak stages are the standard for categorizing AD development based on the degeneration of specific brain regions. Table 1 summarizes tau propagation on a macroscopic scale, on the order of months or even years. Tau pathology starts locally and subcortically in the LC and TEC, and eventually spreads exponentially to cortical structures.

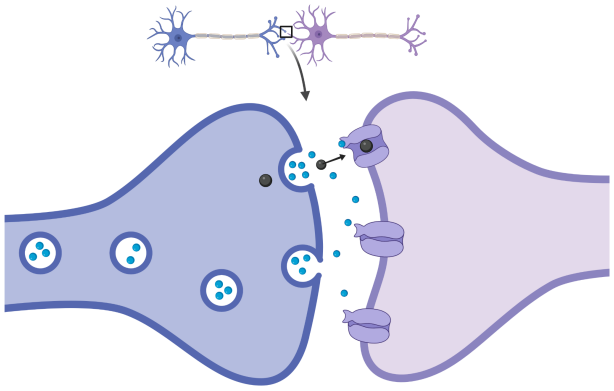

Figure 1: Spread of tau on a microscopic scale, based on the tau propagation hypothesis; Adapted from "Synaptic Cleft (Horizontal)", by BioRender.com (2021). Retrieved from https://app.biorender.com/biorender-templates

According to the tau propagation hypothesis, the neuronal spread of tau occurs (1) upon release from a presynaptic cell[14*]. (2) A "seed" tau traverses a synapse[15**] before (3) its absorption by the postsynaptic cell[17***](Figure 1). Like a seed poised to grow into an uncontrollable weed, the tau begins replicating and taking up room in the cell, until NFTs are pervasive. This is why it is understandable how dementia can ensue as this process repeats *ad infinitum*.

C. Current Therapeutics

Presently, while there is no cure for AD, there are several medications to treat the behavioral symptoms of AD and slow down its progression. However, these medications lose their efficacy over time. The only FDA-approved medications applied for treating AD are memantine, donepezil, rivastigmine, galantamine, and aducanamab[18,19].

Memantine is an N-methyl-D-aspartate receptor antagonist, as it decreases the transmission of the excitatory neurotransmitter, glutamate[19], hindering the spread of tau. Unfortunately, because of glutamate ubiquity, memantine functions at a low level[19]. Donepezil, rivastigmine, and galantamine are collectively termed cholinesterase inhibitors. They inhibit acetylcholinesterase[19], which is an enzyme involved in the breakdown of the neurotransmitter acetylcholine. Acetylcholine is sparse in people with AD, so the medication attempts to make it more abundant; nevertheless, it does not address tau pathology. Lastly, aducanamab is the newest FDA-approved medication, which functions by safeguarding against amyloid-beta (Aβ) peptide[20]. However, multiple aducanamab studies have failed to demonstrate efficacy and there are reports of adverse physiological effects such as swelling and bleeding[21,22].

The current theme with all these medications is that they fail to stop tau propagation. Only recently have researchers focused on several anti-tau therapeutics and some are in development. Regardless, since these therapeutics lack specificity, they do not have an effect on the most vulnerable neuronal networks described in Table 1. And as such, a new targeted treatment paradigm would greatly benefit those suffering from early AD.

D. Developing Therapeutics

Immunotherapies are targeted treatments that engage the body's defense system to fight against aberrant tau[23]. Alas, one such immunotherapy, AADvac1, has failed to report any significant rescue of cognitive function[24]. Another example is ACI-35, which carries synthetic compounds into tissues to eliminate tau. ACI-35 has also been found to be unsuccessful in clinical trials, likely because the immune system was not fully engaged[25]. In principle, immunotherapies are promising but may not be suited to combat the complex mechanisms associated with tau propagation.

* The release can be passive, meaning the presynaptic ion channels are not involved, or active, wherein the presynaptic ion pumps exert a force against a concentration gradient. ** Alternatively, neurons release vesicles called exosomes containing tau[16].
*** Adsorption occurs via endocytosis[17]. This means it is engulfed by the postsynaptic neuron.

Chaperone-mediated autophagy is a cell-cleaning process that recedes with the onset of AD[26]. By the time tau clusters in proteins, chaperone-mediated autophagy has often stopped occurring; thus, it does not remove NFTs[26]. In studies with mice models, using a derivative CA77.1, degradation was reversed *in vivo*[27]. Preliminary testing has shown promise, but the potential clinical application is still years away.

Although these developing treatments hijack innate biological systems, what if an engineering approach could be the pinnacle solution to treating AD based on the phenomenon of tau propagation? Could the body be thought of as a conduit for an anti-tau cure? What form would this treatment take?

E. The Present Study

The current study proposes a novel therapeutic which can treat tau prevalence in AD by targeting the protein's spread. In my previous study, I evaluated the net potency of anti-tau compounds computationally. Parameters for protein removal can be entered into a theoretical model that is based on a modified Watts-Strogatz small-world network[30]. For quicker analysis, they can also be tested against a polynomial support vector machine algorithm which classifies therapeutic agents based on neuronal survival rates[30]. The therapeutic classes are elaborated in Table 2. They should affect 95% of infected cells and reduce tau spreading activity by 85% in order to satisfy the contingency for a Class A therapeutic[30].

Therapeutic Class	Resulting Neuronal Survival Rate
Class A	99-100%
Class B	95-99%
Class C	90-95%
Class D	less than 90%

Table 2: The therapeutic classes and survival rate ranges that define them; adapted from Khalfin & Sbaiti[30]

These therapeutics can be encapsulated in biodegradable nanoparticles (NP) that act as vehicles for synthetic compounds. Such NPs will implement a "Trojan Horse" design optimized for drug delivery across the blood-brain barrier. The present study hypothesized that destructive compounds transported by NPs could significantly terminate the early spread of tau. This novel computational hemodynamics study focused on the theoretical delivery method, whereby the locus coeruleus or transentorhinal cortex can be precisely targeted by a nanoparticle to reverse neurodegeneration in Alzheimer's Disease.

2. Methods

A. Cardiovascular Pathway For Delivery

Several routes of delivery were considered based on their reported bioavailability, a measurement of the NP that successfully enters cardiovascular circulation[32]. Nasal administration was initially favorable due to its proximity to the central nervous system. However, bioavailability was found to be inversely proportional with molecular weight[32] and the absorption surface area was too low[32]. The oral pathway was also eliminated due to its consistently low bioavailability caused by the intestinal epithelial barrier, a significant obstacle to intracerebral localization[33]. An intravenous injection offered complete bioavailability of drugs even with low doses, but potentially risked damage to the heart, lungs, kidney, liver, and spleen tissues[34]. Since transradial injection (arterial) offered complete bioavailability[32] and offered a direct path to the LC or TEC, this route of administration was chosen. Although a transradial injection can be a painful injection, the area can be anesthetized with a subcutaneous anesthetic agent.

Anatomy was a guiding principle while pinpointing the arterial track of NP travel. The LC is found in the hindbrain; the TEC encapsulates the perirhinal area[31], which is found adjacent to the entorhinal and hippocampal regions. Therefore, the procedure seeks to initially puncture the right radial artery through the wrist. Then the NP will flow along the arterial pathway shown in Figure 2.

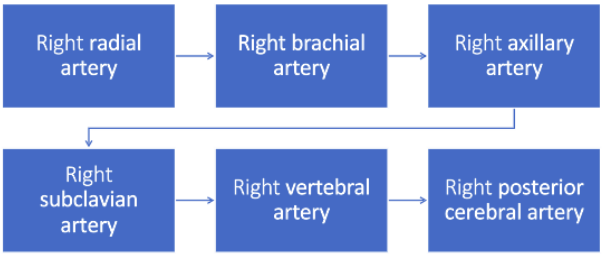

Figure 2: Flowchart of the arterial travel route; referred to as steps 1-6

The rationale for steps 1-5 is that they are favorably connected in human anatomy, as they go toward the brain[35]. Step 6 is a novel step which localizes to the hippocampal region (the nexus to the TEC)[36], where the spread of tau can be terminated[30]. The NP has a hyperphosphorylated tau antibody*, so localization to the LC or TEC is guaranteed by this design.

B. *In Silico* Model

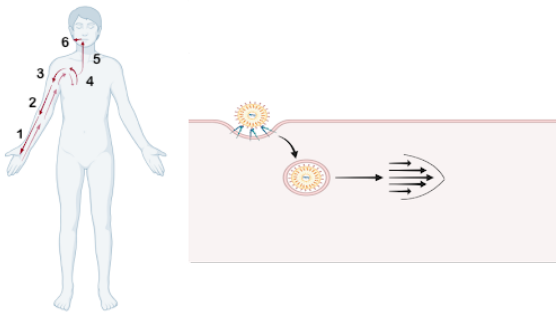

Figure 3: Blood flow in arteries 1-6 shown as an aggregate compared to the ideal flow (left), transradial administration and velocity vectors upon adsorption of NP (right); Adapted from "Solid Lipid Nanoparticle Delivery Pathway", by BioRender.com (2021). Retrieved from https://app.biorender.com/biorender-templates

* Relevant anti-tau antibodies will likely include murine versions of BIIB076 and UCB0107 which have combated tau propagation in vitro[28,29].

Blood flow in arteries 1-4 is in the opposite direction of the proposed delivery path, as seen in Figure 3. Typically, transradial injections targeting the brain implement a catheter, or a hollow straw. The goal in this study was to model the trajectory of a NP in regular bloodflow because this method is noninvasive and quick to action. Nanomotors were simulated in conjunction with the NP, in an effort to counteract blood velocity. Using glucose at 10 * 10^{-3} M, a velocity of about 12 µm/s for 100 nanomotors can be achieved[37]. The order of magnitude required for the blood velocity is in cm/s and the order of magnitude for mean arterial diameter is at least 1 mm. Figure 4 depicts 0.1 mm of nanomotors resulting in a speed of 1 cm/s, which satisfied the general range. These measurements confirmed the feasibility of nanomotors because the required area fits within the diameter or the cross-sectional area of the artery at any moment of time.

$$\frac{10^2 nm}{10\ \mu m/s}\left(\frac{10^4\ \mu m/s}{1\ cm/s}\right)\left(\frac{1\ mm}{10^6\ nm}\right) = 0.1\ mm\ of\ nanomotors\ for\ 1\ cm/s$$

Figure 4: Order of magnitude calculation for nanomotors using factor-label method

To determine the blood velocities in arteries 1-6, Python (version 3.8, Spyder 4 IDE) code was utilized. First, a comprehensive literature review was done on various studies to extract the data found in Table 3. Preference was given to recent studies done in an *in vivo* setting.

	Radial artery	Brachial artery	Axillary artery	Subclavian artery	Vertebral artery	Posterior cerebral artery
Pressure (P) (mmHg)	100.[38*]	120.[38]	130.[38]	140.[38]	60.[38]	50.[38]
Diameter (d) (mm)	2.38[39]	3.97[40]	6.38[41]	7.8[42]	3.02[43]	1.94[44]
Length (L) (mm)	218.1[45]	101.3[46]	101.5[47]	78[48]	38.8[49]	52[50**]
Viscosity (µ) (cP)	4.5[51]	4.5[51]	4.5[51]	4.5[51]	4.5[51]	4.5[51]

Table 3: Parameters in the computational fluid dynamics model, based on mean approximate values
*The number in the superscript is a citation; the peak diastolic arterial pressures were obtained in an interview with a vascular doctor
**This is the full length, not the length to the hippocampal region

Assumptions were made that vasoconstriction, the decrease in arterial diameter and the accompanying systolic pressure caused by smooth muscle contraction, was constant; vasodilation, the increase in arterial diameter and the accompanying diastolic pressure caused by smooth muscle relaxation, was insignificant; blood was a Newtonian fluid, meaning that viscosity was constant[52]; blood flow was approximately centered and confined to one-dimension motion; increasing mass of nanomotors was ultimately negligible; only the plasma portion of blood flow was involved in NP transportation, and other potential interferences were not present; there was negligible shearing pressure (friction).

$$q = \frac{(p_1 - p_2)\pi a^4}{8\mu L}$$

Figure 5: Hagen–Poiseuille equation, where q is the volumetric flow rate, p_1 - p_2 is the systolic arterial pressure gradient, a is the mean arterial radius, μ is the mean blood viscosity, and L is the mean arterial length

Second, the Hagen–Poiseuille equation, displayed in Figure 5, was solved for arteries 1-6 to find the volumetric flow rate, q, in mm^3/s. The code was carried out in *initialVel*, which had appropriate parameter values to plug into the equation. The volumetric flow rate was the volume of fluid flowing along the tube per unit time[52]. The equation was applicable in a Newtonian fluid, and is standardly used to demonstrate the parabolic velocity profile caused by streamlined blood flow[52]. It pertained to this scenario because of the assumptions delineated previously. The radius, a, was determined by applying the formula $a = d/2$ (d is a diameter). Pressures were converted from mmHg to mPa to keep consistent units. The units of volumetric flow rate, q, were derived from a dimensional analysis calculation in Figure 6.

$$[q] = \frac{[\Delta p][\pi][a]^4}{[8][\mu][L]} \rightarrow [q] = \frac{(mPa)(mm)^4}{(mPa)(s)(mm)} \rightarrow [q] = mm^3/s$$

Figure 6: Dimensional analysis of Hagen-Poiseuille equation

Third, the volumetric flow rate, q, was converted to an initial velocity, u_0, by solving the equation $Q = Au_0$ where A was the cross-sectional area found using $A = \pi a^2$. Then the initial velocity, u_0, could be iteratively substituted into a form of Bernoulli's equation contingent on a height differential, dh.

$$\lim_{n \to \infty} \sum_{i=1}^{n} B(h_i)\Delta h = \int_{L_0}^{L} B(h)dh \text{ where } B(h) = P + 0.5\rho u^2 + \rho gh$$

Figure 7: The proposed novel procedure was similar to taking an integral of the Bernoulli function

This could be approximated as the integral of the Bernoulli function, *B(h)*, displayed in Figure 7. The Bernoulli function essentially mirrored a physical representation of the Law of Conservation of Energy. The term $0.5\rho u^2$ was the kinetic energy per unit volume and the term ρgh was the potential energy per unit volume. When the potential energy decreased due to the increasing height, h, multiplied by the negative acceleration due to gravity, g, it was always accompanied by a corresponding increase in the kinetic energy. The translational increase was in the velocity, u, since the density, ρ, was assumed to be constant. Therefore, across all values of the height, the integral of the Bernoulli function was rectangular. Hence, the integral could be calculated as the area under the curve, shown in Figure 8.

$$\int_{L_0}^{L} B(h)dh = B(h0) \cdot \Delta h$$

Figure 8: Calculation of the integral for the Bernoulli function

A differential equation could be solved for the velocity, *u*, by implementing the scikit module in Python. The proposed methodology calculated the velocity, *u*, using systems of equations formed by varying the height differential, *dh*. The system was solved using the steps in Figure 9. The solution did not include the density, ρ, which was eliminated from the the equation. The code was carried out in *bernoulliSolver*.

$$B(h_1) = B(h_2)$$
$$P + 0.5\rho u_0^2 + \rho g h_1 = P + 0.5\rho u^2 + \rho g h_2$$
$$0.5u_0^2 + g h_1 = 0.5u^2 + g h_2$$
$$u = \sqrt{\left| u_0^2 + 2g h_1 - 2g h_2 \right|}$$

Figure 9: Systems of equations solved for the subsequent velocity, u

Although the proposed solution took inspiration from calculus, it was necessary to sidestep the integral since the height could change at variable intervals in arteries 1-6. The arterial pathway could run horizontally, diagonally, or vertically as a function of its mean arterial length, *L*. The model used in this paper does not actually incorporate this fact, as an assumption was made that the mean arterial length, *L*, is equal to the height, *h*. Additionally, a numpy array of equivalentally distributed heights was generated, which divided the height, *h*, into 1000 equal steps for each artery. The *precision* of 1000 steps is a parameter that can vary from simulation to simulation, depending on the preferences of the researcher. The heights were provided by the method *findHeights*. This flexibility in hardcoding the majority of the functionality and making the corresponding github repository public[53] ensured that future work can expand on the model by making it more biologically accurate.

Fourth, the velocities, [[u_{11}, u_{12}, u_{13}, ..., u_{11000}], [u_{21}, u_{22}, u_{23}, ..., u_{21000}], ..., [u_{61}, u_{62}, u_{63}, ..., u_{61000}]], obtained from the Hagen-Poiseuille equation and Bernoulli function were stored in a 2D numpy array in *generateVel*. The final goal of determining the blood velocity was accomplished.

Nevertheless, nanomotors still had to be added to propel the NP in the opposite direction of the blood flow for arteries 1-4. Then, they had to break off and arrive back at the radial artery for extraction following a specified amount of time, $2 \cdot t_{1-4}$. The velocity of the NP was validated using relative motion, because as long as the minimal speed was reached and there was cross-sectional area remaining, a variable amount of nanomotors could be added. Moreover, nanomotor velocity could potentially be increased by varying the glucose concentration. Both variables were simulated and analyzed provided that the nanomotor velocity was a constant of 1 cm/s by 0.1 mm of nanomotors or the amount of nanomotors was a constant of 0.1 mm, respectively. The methods for this task included *addMotors* and *addSpeeds*. The subsequent procedure was applied to realize this task.

$$\bar{v} = \frac{dh}{\Delta t} \rightarrow \Delta t = \frac{dh}{\bar{v}}$$

Figure 10: Average velocity equation rearranged to solve for time

The result obtained by addition of the nanomotor velocity, which was constant for arteries 1-4 and 0 mm/s for arteries 5-6, to each value in the array of blood flow velocities could be considered approximately average velocities over the short interval of time, Δt, required to traverse the height differential, *dh*. The equation shown in Figure 10 naturally stemmed from this assumption. Using the equation, a new numpy array with times, [[t_{11}, t_{12}, t_{13}, ..., t_{11000}], [t_{21}, t_{22}, t_{23}, ..., t_{21000}], ..., [t_{61}, t_{62}, t_{63}, ..., t_{61000}]], was solved. The total sum of these times was computed for each artery yielding a new array of times, [t_1, t_2, t_3, t_4, t_5, t_6]. Finally, the sum of the remaining times was calculated revealing the time variable t_{total} in seconds. In this model, the "optimal" or "desired" value was a low time, t_{total}, which demonstrated sound efficacy and efficiency. All dot plots were generated using the Python module matplotlib. All the code used was made available at the Github repository called *fluid-dynamics-model*[53].

3. Results

A. Varying Amount and Velocity of Nanomotors

Blood Velocity

Variable	Description	Value
blood_vel	Numpy array with the mean peak systolic blood velocities before adding nanomotors	[-3.3, -24, -74, -140, 44, 14] cm/s

Table 4A: Preliminary results; all values are rounded to 2 significant figures

Varying Amount of Nanomotors

Variable	Description	Value
motor_min	Minimum amount of nanomotors necessary to achieve a consistently positive velocity at all points along arteries 1-6	15 mm
$2 \cdot t_{1\text{-}4}$	Total time for nanomotors to travel with NP, then break off from NP, and flow back to delivery site for extraction from blood flow (assuming the value for *motor_min* is used)	33 s
artery_times	Numpy array with the total times for NP travel through each artery (assuming the value for *motor_min* is used)	[1.5, 0.8, 1.3, 13, 0.88, 3.7] s
t_{total}	Total time for NP to work its way to the hippocampal area	21 s

np_vel	Numpy array with the mean NP velocities following the addition of nanomotors (assuming the value for *motor_min* is used; found using *addMotorsVel*)	[150, 130, 76, 6.1, 44, 14] cm/s
motor_amt	Numpy array for the tested lengths of nanomotors, starting from *motor_min* and keeping within biological realism	[15, 18, 21, ..., 95, 98, 100] mm
test_times	Numpy array with the total times for NP travel starting at the right radial artery and ending in the hippocampal brain region	[21, 9.6, 8.2, 7.4, 7.0, 6.7, 6.4, 6.3, 6.1, 6.0, 5.9, 5.8, 5.7, 5.6, 5.6, 5.6, 5.5, 5.5, 5.4, 5.4, 5.3, 5.3, 5.3, 5.3, 5.2, 5.2, 5.2, 5.2, 5.2, 5.2] s

Table 4B: Results obtained from varying the amount of nanomotors, while keeping the speed of the nanomotor, motor_speed, a constant of 1 cm/s per 0.1 mm; all values are rounded to 2 significant figures

Varying Speed of Nanomotors

Variable	Description	Value
motor_speed	Minimum speed of nanomotors necessary to achieve a consistently positive velocity at all points along arteries 1-6	15 cm/s
speed_vals	Numpy array for the tested speeds of nanomotors, starting from *motor_speed* and keeping within biological realism	[15, 18, 21, ..., 95, 98, 100] cm/s
test_times	Numpy array with the total times for NP travel starting at the right radial artery and ending in the hippocampal brain region	[21, 9.6, 8.2, 7.4, 7.0, 6.7, 6.4, 6.3, 6.1, 6.0, 5.9, 5.8, 5.7, 5.6, 5.6, 5.6, 5.5, 5.5, 5.4, 5.4, 5.3, 5.3, 5.3, 5.3, 5.2, 5.2, 5.2, 5.2, 5.2, 5.2] s

Table 4C: Results obtained from varying the speed of nanomotors, while keeping the amount of nanomotors, *motor_area*, a constant of 0.1 mm; all values are rounded to 2 significant figures

In the model, the positive direction represented the pathway of an anti-tau NP moving toward the TEC. The mean peak systolic blood velocities, *blood_vel*, had negative values in arteries 1-4, as evidenced by Table 4A. This was expected and provided the rationale for adding nanomotors. The minimum amount of nanomotors, *motor_min* (Table 4B), was equivalent to the minimum NP speed, *motor_speed* (Table 4C), to achieve a constant positive velocity along the arterial path. As a consequence, the amounts of nanomotors, *motor_amt* (Table 4B), equaled the speeds of nanomotors, *speed_vals* (Table 4C); furthermore, the total times for NP travel, *test_times* (Tables 4B; 4C) were exactly alike. The minimum amount of nanomotors seemed to be an outlier value (Figure 11). There was approximately exponential decay, culminating in an asymptomatic trend toward 5 seconds for infinitely large amounts of nanomotors.

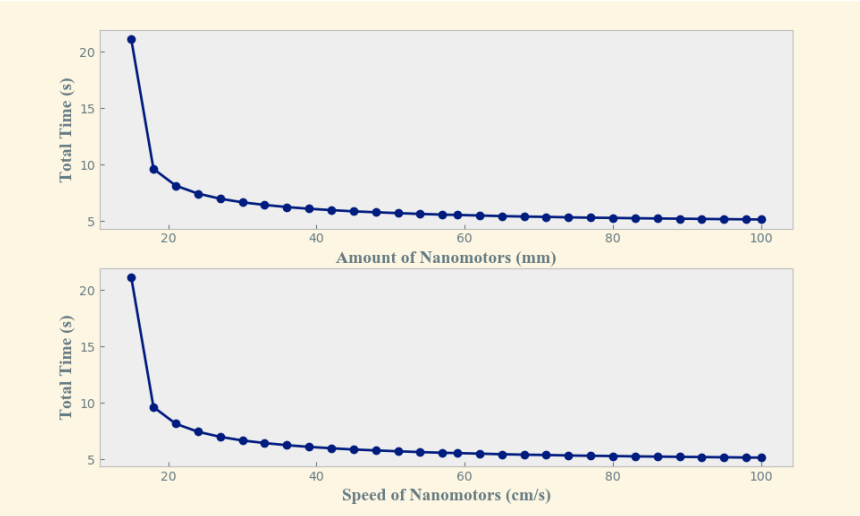

Figure 11: The amount of nanomotors as the independent variable and the total time as the dependent variable (Top); the speed of nanomotors as the independent variable and the total time as the dependent variable (Bottom)

The average total time after a slight deviation in nanomotors, μ_T, was compared to the total time at the minimum amount of nanomotors, t_{total} (Table 4B), using a one sample t-test (H_0: $\mu_T = motor\_min$, H_A: $\mu_T < motor\_min$). All conditions for analysis were met as shown in Figure 12.

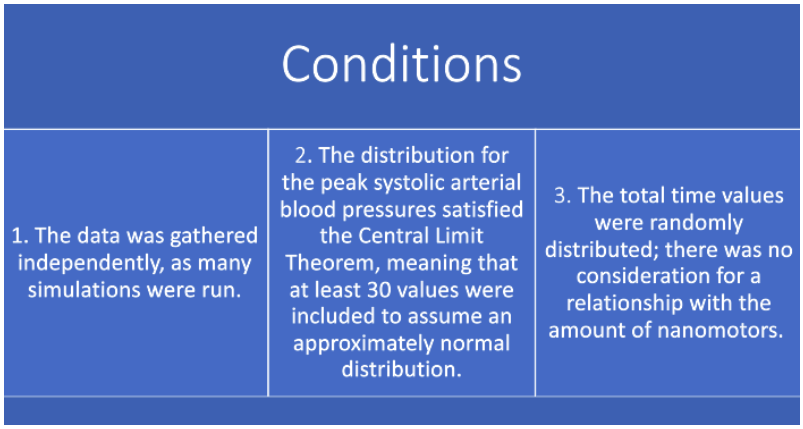

Figure 12: The conditions for a one sample t-test were met.

In Python, the statistical analyses revealed that t = -80.114 and p < .001. Because the p-value was less than α = 0.01, the conclusion was made that using an amount of nanomotors greater than 18 mm was beneficial for achieving a total time of at least 9.6 seconds. The determination was also pertainable to the effect varying speeds of nanomotors had on time since the data was equivalent.

Besides the trajectory of the NP, the total time for the nanomotors to traverse arteries 1-4, break off the NP, and travel back to the wrist for extraction, $2 \cdot t_{1\text{-}4}$ (Table 4B), was 33 seconds. Nanomotors could potentially be reused with multiple anti-tau NPs.

B. *In Vivo* Confirmation

Upon further exploration, an interview with a vascular radiologist was conducted in order to examine the validity of the proposed NP arterial travel[54*]. He provided average peak systolic blood velocities in arteries 1-5 that were seen in healthy individuals, assuming there were no prior complications (Table 5)[54]. This information was used to find the actual NP travel time per artery, assuming regular speed of nanomotors, *motor_speed* (Table 4B), and minimum amount of nanomotors, *motor_min* (Table 4B). A percent error was computed in order to evaluate the accuracy of the model, with the formula $\delta = \left|\frac{v_A - v_E}{v_E}\right| \cdot 100$, where v_A was the actual value and v_E was the estimated value.

Name of Artery	Peak Systolic Velocity	NP Time	Percent Error
Right radial	43.2 cm/s	1.1 s	$\delta = \left\|\frac{1.1\ s - 1.5\ s}{1.5\ s}\right\| \cdot 100 \ -> \ \delta = 27\%$
Right brachial	56.6 cm/s	.49 s	$\delta = \left\|\frac{.49\ s - 0.8\ s}{0.8\ s}\right\| \cdot 100 \ -> \ \delta = 39\%$
Right axillary	85.6 cm/s	.43 s	$\delta = \left\|\frac{.43\ s - 1.3\ s}{1.3\ s}\right\| \cdot 100 \ -> \ \delta = 67\%$
Right subclavian	94.3 cm/s	.83 s	$\delta = \left\|\frac{.83\ s - 13\ s}{13\ s}\right\| \cdot 100 \ -> \ \delta = 94\%$
Right vertebral	69.8 cm/s	.56 s	$\delta = \left\|\frac{.56\ s - .88\ s}{.88\ s}\right\| \cdot 100 \ -> \ \delta = 36\%$

Table 5: Peak systolic blood velocity measured by Philips iU22 Ultrasound Machine

The mean systolic arterial velocity was likely skewed by the model's assumptions, causing the arterial travel times to be different. Blood flow is not actually centered and limited to 1D motion, nor is blood a perfect Newtonian fluid; in addition, systolic pressure, diameter, length, and viscosity can deviate depending on a person's anatomy. The model takes these values as parameters, so they can be edited to develop more personalized medicine for treating AD.

4. Discussion

As hypothesized, anti-tau NPs can travel to the LC or TEC in order to halt tau propagation. The model displayed the time for arterial travel, along with the minimum amount and speed of nanomotors. It predicted the arterial travel time of the proposed NP, which was on the order of seconds. Although the *in vivo* confirmation found high percent errors, the discrepancy with the *in silico* model was not significant as there would still be biological realism, fast onset of action, and high bioavailability.

The model was developed and applied in accordance with biological realism. Namely, all the peak systolic arterial pressures were obtained in an interview with a vascular doctor[38]. Both the Hagen-Poiseuille and Bernoulli equations were standard in the field of hemodynamics[52]. When varying

* The student researcher performed no diagnostic testing.

the amount or speed of nanomotors, the NP velocities were kept in the order of cm/s and confined to 1D motion, to prevent structural damage to arterial walls or the non-plasma part of blood flow, including leukocytes, erythrocytes, and platelets.

$$Amount\ of\ substance\ delivered\ \sim \frac{T_{\frac{1}{2}}}{T_{max}}$$

Figure 13: Predicted relationships between the amount of a substance delivered, its half-life, $T_{\frac{1}{2}}$, and onset of action, T_{max}

The results could be understood in the context of pharmacokinetics, or the movement of drugs. The onset of action of a compound is the duration of time from administration to steady-state. FDA-approved treatments and developing solutions for AD have a longer onset of action when compared to the proposed NP. For example, memantine, donepezil, and CA77.1 reach peak concentrations in 3-7 hours[55], 3-4 hours[56], and 1 hour[27] respectively. But in the hemodynamics model, the attachment of nanomotors resulted in NP arterial travel on the order of seconds. The shorter onset of action is favorable because the substance goes into effect faster. It is also beneficial because the quantity delivered to the brain is larger (Figure 13).

Another pharmacokinetic variable is the half-life of a substance, or the time required for 50% of its decay. CA77.1 has a half-life of 1.89 hours, which curtails the amount that actually gets into the brain[27]. When the half-life of a NP-encapsulated compound is longer, more of it reaches the target region (Figure 13). The design and materials that compose the NP should keep this in mind.

A. Limitations

An important limitation of this model was the omission of increasing mass of the nanoparticle due to the attachment of nanomotors. In the model, mass did not impact the kinematics of NP arterial travel because the shearing pressure was not considered. Shearing pressure is similar to friction in that it denotes opposing "stress" on an object. The equation in Figure 14 can be used to calculate the shearing pressure as a function of the NP's mass, the derivative of velocity taken with respect to time, and the radius.

$$\tau = \frac{F}{A} \rightarrow \tau = \frac{m \cdot \frac{du}{dt}}{\pi a^2}$$

Figure 14: Equation for the shearing pressure in blood flow

The relationship was paradoxical in the current procedure because in order to calculate the shearing pressure, the velocities were needed. However, these variables were not calculated until midway through the design process. As such, future work may want to modify the existing model in order to calculate the shearing pressure using a different equation.

Although the length to the hippocampal region was not accessible, functional magnetic resonance imaging and magnetic resonance angiography could trace blood flow in the brain, which could be used to calculate the length from the start of the right posterior cerebral artery to the TEC. The difference in length was not imperatively consequential because the total time would only be lower, making the NP travel even more efficient.

Another limitation was computational power, which negatively impacted the precision. In the model code, the height differential, *dh*, was manually set as 1000. With greater processing capacity, this value could be markedly higher. Alternatively, the simulations could be run in parallel rather than in serial to increase the efficiency of this model. Still, the increase in iterations would lead to subtle differences. The travel time would be similar; hence, the goal of implementing the theoretical delivery method would not be seriously impacted.

Hemodynamics relies upon models which can marginally differ from reality. In this model, significant figures were used in accordance with standard scientific practices. However, implementing degrees of freedom — the number of digits that a scientific experiment can vary — can potentially reduce rounding errors[57].

B. Future Work

The proposed NP would work on numerous tauopathies other than AD, including progressive supranuclear palsy, Parkinson's disease, and Pick's disease[58]. Such tauopathies originate in different parts of the brain, so the arterial delivery pathway may have to change. There is even a general applicability to disease and injury as long as the transradial delivery method is stipulated. The NP can encapsulate other compounds that are not anti-tau, but would benefit from optimal bioavailability, quick onset of action, and avoidance of the heart, lungs, kidney, liver, and spleen tissues. Implementing new arterial delivery routes would be straightforward using the approach in the present study.

Engineering design constraints will include using the minimum amount or velocity of nanomotors to make transradial delivery via blood flow possible. Altering the velocity of nanomotors is not feasible currently, but adequate technology should be researched. Flexibility in varying a combination of the amount and speed of nanomotors will make future research more versatile, by pulling from optimization algorithms in the fields of linear programming, differential calculus, and graph theory.

The performance of the NP will depend on its external composition, so future research will have to expand on possible biomaterials to guide the design process. For example, polymeric NPs are notable for their biocompatibility and biodegradability[32], and may include polylactide–polyglycolide copolymers, polycaprolactones, polylactic acid, or poly lactic-co-glycolic acid. An anti-tau compound that is encapsulated in a polymeric nanocarrier can be released by diffusion or forceful detachment after arterial

traversal[32]. Another relevant biomaterial may be the hydrogel chitosan, which is already FDA-approved and compatible with various compounds for proper encapsulation[59]. Chitosan's affinity for other materials stems from its primary hydroxyl and amino groups[59]. Biomaterials will need to be evaluated based on their capacity for smooth delivery, as illustrated by the model.

In order to ultimately treat AD, understanding Aβ and its relationship to tau pathology may strengthen compound design. Aβ is a fragment of the Amyloid Precursor Protein, which is normally involved in synapse formation and neuronal plasticity. Contrary to tau, aberrant Aβ is active in the extracellular space between neurons[12], where it accumulates to form amyloid plaques[6] that interfere with neuronal signaling. Some studies report that Aβ enhances tau pathology[60] and initiates a positive feedback loop with tau[61]. The carrier NP can be designed to encapsulate both anti-tau and anti-Aβ compounds for more holistic and comprehensive therapy.

In direct continuation of the present study, future work will involve a third computational model based on high-resolution chemistry to evaluate the actual mechanism of tau removal. Due to NFTs' chemical structure[9], it may be advantageous to simulate the separation of paired helical filaments from single filaments. Additionally, because NFTs are inert[9], employing chemical reactions will be challenging. This process will occur in the extracellular space to avoid neuronal damage. After the completion of this series, anti-tau NPs will become a potential treatment method, poised to be tested with in vivo laboratory experiments.

5. Conclusion

The present work focused on using a hemodynamic computational model to show the trajectory of a carrier NP that encapsulates an anti-tau compound. A transradial injection was selected as the delivery method and an arterial pathway was found. The model simulated the attachment of nanomotors, revealing several descriptive variables that demonstrated efficacy. It favorably showed biological feasibility and required minimal invasiveness.

All of these studies support the development and implementation of the proposed NP in a way that offers a practical cure to AD. Cognitive deficiencies in language, memory, communication, and thinking can be rectified, benefiting individuals with AD and restoring hope to their families.

6. Appendices

Appendix 1 - Nanoparticle Security

A. Cryptography

Although the nanoparticle's hardware and software will be determined sometime in the future, it will most likely be connected to the Internet of Things. This will make it vulnerable to cyberattacks[62]. One way of countering this threat will be to employ a unique cryptographic system.

Cryptography is the art and science of keeping information secure from unauthorized access by using encryption, or encoding it[63]. In modern cryptography, security is not dependent on the secrecy of the encryption method or algorithm, but only on the secrecy of keys[64]. New cipher technology is rooted in complex number theory, specifically modular arithmetic and the application of prime numbers.

B. RSA Encryption

Encryption uses a specific key to map a message to a ciphertext message[65]. Decryption is the process of decoding a message and relies on applying either the same key or a different key[65]. In RSA Encryption, the keys used for encryption and decryption connect[64]. Information security is related to modular exponentiation. A number is raised to an exponent and divided by a modulus, outputting a remainder. This remainder is irreversible. Given the exponent, modulus, and remainder obtained, the original number cannot be derived. In other words, *c* cannot be decrypted without knowing the original number, *A* (Figure 15A).

$$A^e \ (mod\ N) \equiv c$$

Figure 15A: Encryption congruence

However, a person who has access to the original number could work backward to obtain it again. Letting *d* equal an integer, the original number, *A*, can be found (Figure 15B).

$$c^d \ (mod\ N) \equiv A$$

Figure 15B: Decryption congruence

Then, applying the property of modular exponentiation, a new equation can be found (Figure 15C).

$$A^{ed} \ (mod\ N) \equiv A$$

Figure 15C: Encryption and decryption congruence combined

That is a surefire way to reverse the exponentiation. So, RSA Encryption relies on a reliable (replicable, accurate) algorithm to generate a number, *d*.

The optimal way to do this involves Euler's totient function, ϕ, a high-order arithmetic function prevalent in number theory[64]. The totient function denotes the number of positive integers relatively prime to a number, *N*. It relies on knowing the prime factorization, which will always involve 2 prime factors.

$\forall N = p \cdot q \Rightarrow \phi(p,q) = (p-1)(q-1)$ under all circumstances where *p* and *q* are prime. Finding a number's prime factorization is a fundamentally hard problem, but multiplying p and q is simple even for large inputs. Therein lies the key to RSA Encryption.

First, start with Euler's Theorem (Figure 16).

$$A^{\phi(N)} \equiv 1 \ (mod\ N)$$

Figure 16: Euler's Theorem

Then, manipulate using modular multiplication and exponential properties (Figure 17A).

$$A^{k\phi(N)} \equiv 1 \ (mod\ N) \Rightarrow A \cdot A^{k\phi(N)} \equiv A \ (mod\ N) \Rightarrow A^{k\phi(N)+1} \equiv A \ (mod\ N)$$

Figure 17A: Derivation of new formula; this is an intermediate step

This process yields an equation for finding *e*. Remember the original equation (Figure 15C). Now, set the exponent portions of the congruences equal (Figure 17B).

$$ed = k\phi(N) + 1$$

Figure 17B: Derivation of new formula; this is an intermediate step

Divide by *e* on both sides. The final equation for *d* is as follows (Figure 17C).

$$d = \frac{k\phi(N)+1}{e}$$

Figure 17C: Derivation of the formula for the number *d*

Without knowing the original numbers multiplied together, *p* and *q*, an infiltrator to the system could not compute the totient function. Going the other way (from the receiving party to the encryptor) relies on the power of the congruence equation. Both have irreversibility that makes this system so secure.

A simple example will show RSA Encryption in action. Imagine an engineer, John, interested in communicating with a doctor, Helen. John generates 2 random prime numbers: $p = 59$ and $q = 71$. Next, he multiplies them together to get $N = 4189$. This operation is easy to do but challenging to reverse. $\phi(4189)$ is comparable to doing $\phi(59) \cdot \phi(71)$, resulting in a number $(59-1)(71-1) = 4060$. John picks an exponent $e = 9$. He computes *d* by applying the formula from Figure 17C: $d = \frac{8\phi(4189)+1}{9} = 3609$. In this case, $k = 8$ because this is the only value that makes *d* a whole number. After doing these steps, he is ready to send information over to Helen.

John has to send Helen *N* and *e* and omit *p*, *q*, *k*, and *d*. Helen wants to send John a secret message *A*, a string of characters converted to a number. Assume $A = 73$. She does this by computing according to the relationship from Figure 15A. She gets 3636 for her encryption, *c*, which she sends back to John. Now, figuring out the message is easier for John. He applies the formula from Figure 15B. Surely

enough, *A* is 73, which is what Helen sent. Despite the mathematical manipulation, the result is still the same.

My novel idea for a new cryptographic system has its basis in an RSA network[64]. Its goal will be to support a large cryptographic cluster, resembling something of the following nature (Figure 18).

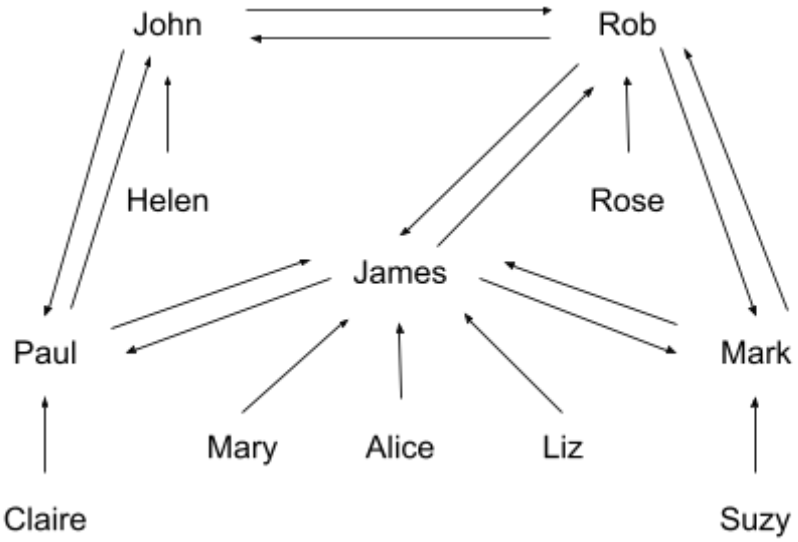

Figure 18: Dense cryptonetwork; the goal is to foster global communication to speed the process of nanoparticle development, allow for fine-tuning based on anatomy, and make quick adjustments in a live setting, all while keeping hackers at a safe distance

C. Connecting Cryptosystems

In the future, it is imperative that people have slightly different nanoparticles based on their body anatomy. As such, cryptographers will want to share data securely to treat AD patients worldwide.

With the model explored above, only one person has access to the key. However, that one person can receive information from many sources. Perhaps there is a different situation where there are two keyholders from different cryptosystems. In that case, they may each define their keys according to the specific moduli, N_1, and N_2.

The Chinese Remainder Theorem can apply when building interlinking congruence structures. Expanding on the example above, suppose that an engineer, John, has a doctor-client, Helen, and another engineer, Rob, has a doctor-client, Rose. Then, they may each define RSA cryptosystems using random number generators for inputs, p_1, q_1 p_2, and q_2, respectively. Keeping the data the same for John and Helen's communication and adding data for Rob and Rose's communication, the following calculations will occur (Table 6).

Exchange between John and Helen	Exchange between Rob and Rose
$p_1 = 59$	$p_2 = 103$

$q_1 = 71$	$q_2 = 113$
$e_1 = 9$	$e_2 = 5$
$N_1 = 4189$	$N_2 = 103 \cdot 113$ $N_2 = 11639$
$d_1 = 3609$	$\phi(11639) = 11424$ $d_2 = \frac{11424 + 1}{5}$ $d_2 = 2285$
$A_1 = 73$	$A_2 = 119$
$c_1 = 3636$	$119^5 \pmod{11639} \equiv c_2$ $c_2 = 1787$ $1787^{2285} \pmod{11639} \equiv 119$

Table 6: Exchanges in unique RSA cryptosystems

At first, calculations pertain to each cryptosystem independently. Still, 2 cryptosystems were developed, each with viable data. They should interact with one another (Figure 18).

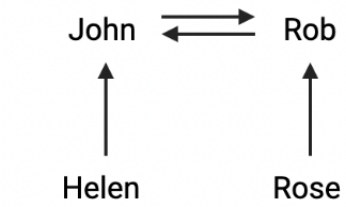

Figure 18: Visualization of a small cryptonetwork with two parties

Now the Chinese Remainder Theorem can be used to combine that data into an overarching cryptosystem. The system of congruence equations will be the following (Figure 19A).

$$x \equiv 119 \ (mod\ 1163);\ x \equiv 73 \ (mod\ 4189)$$

Figure 19A: Congruences to apply the Chinese Remainder Theorem

Using the Extended Euclidean Algorithm and various properties of moduli, this is a description of how both parties could communicate (Figure 19B).

$$P_1 = 4189,\ P_2 = 11639$$

$$4189Q_1 \equiv 1 \pmod{11639}$$
$$11639Q_2 \equiv 1 \pmod{4189}$$

$$11639 = 4189 \cdot 2 + 3261$$
$$4189 = 3261 \cdot 1 + 928$$
$$3261 = 928 \cdot 3 + 477$$
$$928 = 477 \cdot 1 + 451$$
$$477 = 451 \cdot 1 + 26$$
$$451 = 26 \cdot 17 + 9$$
$$26 = 9 \cdot 2 + 8$$
$$9 = 8 \cdot 1 + 1$$
$$8 = 1 \cdot 8 + 0$$

$$3261 = 11639 - 4189 \cdot 2 = b - 2a$$
$$928 = a - (b - 2a) = 3a - b$$
$$477 = (b - 2a) - 3(3a - b) = 4b - 11a$$
$$451 = (3a - b) - (4b - 11a) = 14a - 5b$$
$$26 = (4b - 11a) - (14a - 5b) = 9b - 25a$$
$$9 = (14a - 5b) - 17(9b - 25a) = 439a - 158b$$
$$8 = (9b - 25a) - 2(439a - 158b) = 325b - 903a$$
$$1 = (439a - 158b) - (325b - 903a) = 1342a - 483b$$
$$1 = 1342 \cdot 4189 - 483 \cdot 11639$$

$$(1342)(4189) \equiv 1 \pmod{11639}$$
$$Q_1 \equiv 1342 \pmod{11639}$$

$$11639Q_2 \equiv 1 \pmod{4189}$$
$$3261Q_2 \equiv 1 \pmod{4189}$$

$$4189 = 3261 \cdot 1 + 928$$
$$3261 = 928 \cdot 3 + 477$$
$$928 = 477 \cdot 1 + 451$$
$$477 = 451 \cdot 1 + 26$$
$$451 = 26 \cdot 17 + 9$$
$$26 = 9 \cdot 2 + 8$$
$$9 = 8 \cdot 1 + 1$$
$$8 = 1 \cdot 8 + 0$$

$$928 = 4189 - 3261 = b - a$$
$$477 = a - 3(b - a) = 4a - 3b$$
$$451 = (b - a) - (4a - 3b) = 4b - 5a$$
$$26 = (4a - 3b) - (4b - 5a) = 9a - 7b$$
$$9 = (4b - 5a) - 17(9a - 7b) = 123b - 158a$$
$$8 = (9a - 7b) - 2(123b - 158a) = 325a - 253b$$
$$1 = (123b - 158a) - (325a - 253b) = 376b - 483a$$
$$1 = 376 \cdot 4189 - 483 \cdot 3261$$

$$(-483)(3261) \equiv 1 \pmod{4189}$$
$$(3706)(3261) \equiv 1 \pmod{4189}$$
$$Q_2 \equiv 3706 \pmod{4189}$$

$$x \equiv 119 \cdot 4189 \cdot 1342 + 73 \cdot 11639 \cdot 3706 \pmod{48755771}$$
$$x \equiv 14816566 \pmod{48755771}$$

Figure 19B: Calculations bridging the 2 cryptosystems which could be repeated many times in a cryptonetwork

Works Cited

1. National Collaborating Centre for Mental Health (UK). Dementia. Dementia: A NICE-SCIE Guideline on Supporting People With Dementia and Their Carers in Health and Social Care. 2007. Available from: https://www.ncbi.nlm.nih.gov/books/NBK55480/
2. Meiland FJ, Kat MG, Van Tilburg W, Jonker C, Dröes RM. The emotional impact of psychiatric symptoms in dementia on partner caregivers: do caregiver, patient, and situation characteristics make a difference? Alzheimer Disease & Associated Disorders. 2005 Oct 1;19(4):195-201. doi: 10.1097/01.wad.0000189035.25277.02
3. Tagariello P, Girardi P, Amore M. Depression and apathy in dementia: same syndrome or different constructs? A critical review. Archives of gerontology and geriatrics. 2009 Sep 1;49(2):246-9. Available from: https://doi.org/10.1016/j.archger.2008.09.002
4. Kelley AS, McGarry K, Bollens, Lund E, Rahman OK, Husain M, Ferreira KB, Skinner JS. Residential setting and the cumulative financial burden of dementia in the 7 years before death. Journal of the American Geriatrics Society. 2020 Jun;68(6):1319-24. Available from: https://doi.org/10.1111/jgs.16414
5. Alzheimer's Association. 2019 Alzheimer's disease facts and figures. *Alzheimer's & Dementia*. 2019 Mar;15(3):321-87. Available from: https://doi.org/10.1016/j.jalz.2019.01.010
6. Ramirez-Bermudez J. Alzheimer's disease: critical notes on the history of a medical concept. *Archives of Medical Research*. 2012 Nov 1;43(8):595-9. Available from: https://doi.org/10.1016/j.arcmed.2012.11.008
7. Kim E, Otgontenger U, Jamsranjav A, Kim SS. Deleterious alteration of Glia in the brain of Alzheimer's disease. *International Journal of Molecular Sciences*. 2020 Jan;21(18):6676. Available from: https://doi.org/10.3390/ijms21186676
8. Hampel H, Mesulam MM, Cuello AC, Khachaturian AS, Vergallo A, Farlow MR, Snyder PJ, Giacobini E, Khachaturian ZS. Revisiting the cholinergic hypothesis in Alzheimer's disease: emerging evidence from translational and clinical research. *The Journal of Prevention of Alzheimer's Disease*. 2019 Jan;6(1):2-15. Available from: https://link.springer.com/article/10.14283/jpad.2018.43
9. Iqbal K, Liu F, Gong CX, Grundke-Iqbal I. Tau in Alzheimer disease and related tauopathies. Current Alzheimer Research. 2010 Dec 1;7(8):656-64. Available from: https://doi.org/10.2174/156720510793611592
10. Naseri NN, Wang H, Guo J, Sharma M, Luo W. The complexity of tau in Alzheimer's disease. *Neuroscience Letters*. 2019 Jul 13;705:183-94. Available from: https://doi.org/10.1016/j.neulet.2019.04.022

11. Noble W, Hanger DP, Miller CC, Lovestone S. The importance of tau phosphorylation for neurodegenerative diseases. *Frontiers in Neurology*. 2013 Jul 1;4:83. Available from: https://doi.org/10.3389/fneur.2013.00083
12. Alzheimer's Association. Tau Topic Sheet. *Azlheimer's & Dementia*. 2021 Oct. Available from: https://www.alz.org/media/Documents/alzheimers-dementia-tau-ts.pdf
13. Vogel JW, Iturria-Medina Y, Strandberg OT, Smith R, Levitis E, Evans AC, Hansson O. Spread of pathological tau proteins through communicating neurons in human Alzheimer's disease. *Nature Communications*. 2020 May 26;11(1):1-5. Available from: https://www.nature.com/articles/s41467-020-15701-2
14. Yamada K, Holth JK, Liao F, Stewart FR, Mahan TE, Jiang H, Cirrito JR, Patel TK, Hochgräfe K, Mandelkow EM, Holtzman DM. Neuronal activity regulates extracellular tau in vivo. *Journal of Experimental Medicine*. 2014 Mar 10;211(3):387-93. Available from: https://doi.org/10.1084/jem.20131685
15. Frost B, Jacks RL, Diamond MI. Propagation of tau misfolding from the outside to the inside of a cell. *Journal of Biological Chemistry*. 2009 May 8;284(19):12845-52. Available from: https://doi.org/10.1074/jbc.M808759200
16. Wang Y, Balaji V, Kaniyappan S, Krüger L, Irsen S, Tepper K, Chandupatla R, Maetzler W, Schneider A, Mandelkow E, Mandelkow EM. The release and trans-synaptic transmission of Tau via exosomes. *Molecular Neurodegeneration*. 2017 Dec;12(1):1-25. Available from: https://molecularneurodegeneration.biomedcentral.com/articles/10.1186/s13024-016-0143-y
17. Takeda S. Tau propagation as a diagnostic and therapeutic target for dementia: potentials and unanswered questions. *Frontiers in Neuroscience*. 2019 Dec 13;13:1274. Available from: https://doi.org/10.3389/fnins.2019.01274
18. National Institute for Health and Clinical Excellence (Great Britain). Donepezil, Galantamine, Rivastigmine and Memantine for the Treatment of Alzheimer's Disease: Review of NICE Technology Appraisal Guidance 111. National Institute for Health and Clinical Excellence; 2011. Available from: https://www.nice.org.uk/guidance/ta217/resources/donepezil-galantamine-rivastigmine-and-memantine-for-the-treatment-of-alzheimers-disease-pdf-82600254699973
19. Atri A. Current and future treatments in Alzheimer's disease. *InSeminars in Neurology* 2019 Apr (Vol. 39, No. 02, pp. 227-240). Thieme Medical Publishers. Available from: https://www.thieme-connect.com/products/ejournals/html/10.1055/s-0039-1678581

20. Sevigny J, Chiao P, Bussière T, Weinreb PH, Williams L, Maier M, Dunstan R, Salloway S, Chen T, Ling Y, O'Gorman J. The antibody aducanumab reduces Aβ plaques in Alzheimer's disease. *Nature*. 2016 Sep;537(7618):50-6. Available from: https://www.nature.com/articles/nature19323
21. Knopman DS, Perlmutter JS. Prescribing Aducanumab in the Face of Meager Efficacy and Real Risks. *Neurology*. 2021 Sep 14;97(11):545-7. Available from: https://doi.org/10.1212/WNL.0000000000012452
22. Knopman DS, Jones DT, Greicius MD. Failure to demonstrate efficacy of aducanumab: An analysis of the EMERGE and ENGAGE trials as reported by Biogen, December 2019. *Alzheimer's & Dementia*. 2021 Apr;17(4):696-701. Available from: https://doi.org/10.1002/alz.12235
23. Novak P, Zilka N, Zilkova M, Kovacech B, Skrabana R, Ondrus M, Fialova L, Kontsekova E, Otto M, Novak M. AADvac1, an active immunotherapy for Alzheimer's disease and non Alzheimer Tauopathies: an overview of preclinical and clinical development. *The Journal of Prevention of Alzheimer's Disease*. 2019 Jan;6(1):63-9. Available from: https://doi.org/10.14283/jpad.2018.45
24. Novak P, Kovacech B, Katina S, Schmidt R, Scheltens P, Kontsekova E, Ropele S, Fialova L, Kramberger M, Paulenka-Ivanovova N, Smisek M. ADAMANT: a placebo-controlled randomized phase 2 study of AADvac1, an active immunotherapy against pathological tau in Alzheimer's disease. *Nature Aging*. 2021 Jun;1(6):521-34. Available from: https://www.nature.com/articles/s43587-021-00070-2
25. Jadhav S, Avila J, Schöll M, Kovacs GG, Kövari E, Skrabana R, Evans LD, Kontsekova E, Malawska B, de Silva R, Buee L. A walk through tau therapeutic strategies. *Acta Neuropathologica Communications*. 2019 Dec;7(1):1-31. Available from: https://doi.org/10.1186/s40478-019-0664-z
26. Kaushik S, Cuervo AM. The coming of age of chaperone-mediated autophagy. *Nature Reviews Molecular Cell Biology*. 2018 Jun;19(6):365-81. Available from: https://doi.org/10.1038/s41580-018-0001-6
27. Bourdenx M, Martín-Segura A, Scrivo A, Rodriguez-Navarro JA, Kaushik S, Tasset I, Diaz A, Storm NJ, Xin Q, Juste YR, Stevenson E. Chaperone-mediated autophagy prevents collapse of the neuronal metastable proteome. *Cell*. 2021 May 13;184(10):2696-714. Available from: https://doi.org/10.1016/j.cell.2021.03.048
28. Nobuhara CK, DeVos SL, Commins C, Wegmann S, Moore BD, Roe AD, Costantino I, Frosch MP, Pitstick R, Carlson GA, Hock C. Tau antibody targeting pathological species blocks neuronal

uptake and interneuron propagation of tau in vitro. *The American Journal of Pathology*. 2017 Jun 1;187(6):1399-412. Available from: https://doi.org/10.1016/j.ajpath.2017.01.022

29. Courade JP, Angers R, Mairet-Coello G, Pacico N, Tyson K, Lightwood D, Munro R, McMillan D, Griffin R, Baker T, Starkie D. Epitope determines efficacy of therapeutic anti-Tau antibodies in a functional assay with human Alzheimer Tau. *Acta Neuropathologica*. 2018 Nov;136(5):729-45. Available from: https://doi.org/10.1007/s00401-018-1911-2
30. Khalfin M, Sbaiti B. A Computational Model of the Trans-Synaptic Spread of Pathogenic Tau in Early Alzheimer's Disease. *IMPULSE - The Premier Undergraduate Neuroscience Journal*. 2021 Dec. Available from: https://impulse.appstate.edu/sites/impulse.appstate.edu/files/Sbati%20et%20al%20(2021).pdf
31. Taylor KI, Probst A. Anatomic localization of the transentorhinal region of the perirhinal cortex. *Neurobiology of Aging*. 2008 Oct 1;29(10):1591-6. Available from: https://doi.org/10.1016/j.neurobiolaging.2007.03.024
32. Chenthamara D, Subramaniam S, Ramakrishnan SG, Krishnaswamy S, Essa MM, Lin FH, Qoronfleh MW. Therapeutic efficacy of nanoparticles and routes of administration. *Biomaterials Research*. 2019 Dec;23(1):1-29. Available from: https://doi.org/10.1186/s40824-019-0166-x
33. Li N, Li XR, Zhou YX, Li WJ, Zhao Y, Ma SJ, Li JW, Gao YJ, Liu Y, Wang XL, Yin DD. The use of polyion complex micelles to enhance the oral delivery of salmon calcitonin and transport mechanism across the intestinal epithelial barrier. *Biomaterials*. 2012 Dec 1;33(34):8881-92. Available from: https://doi.org/10.1016/j.biomaterials.2012.08.047
34. Yang Y, Bao H, Chai Q, Wang Z, Sun Z, Fu C, Liu Z, Liu Z, Meng X, Liu T. Toxicity, biodistribution and oxidative damage caused by zirconia nanoparticles after intravenous injection. *International Journal of Nanomedicine*. 2019;14:5175. doi: 10.2147/IJN.S197565
35. Zalocar LA, Doroszuk G, Goland J. Transradial approach and its variations for neurointerventional procedures: Literature review. *Surgical Neurology International*. 2020;11. doi: 10.25259/SNI_366_2020
36. Perosa V, Priester A, Ziegler G, Cardenas-Blanco A, Dobisch L, Spallazzi M, Assmann A, Maass A, Speck O, Oltmer J, Heinze HJ. Hippocampal vascular reserve associated with cognitive performance and hippocampal volume. *Brain*. 2020 Feb 1;143(2):622-34. Available from: https://doi.org/10.1093/brain/awz383
37. Guix M, Weiz SM, Schmidt OG, Medina Sánchez M. Self propelled micro/nanoparticle motors. *Particle & Particle Systems Characterization*. 2018 Feb;35(2):1700382. Available from: https://doi.org/10.1002/ppsc.201700382

38. Mark, R. Systolic Blood Pressure Consultation. [Personal interview, 27 Oct] Freeport, NY; 2021 (Unpublished).
39. Yan ZX, Zhou YJ, Zhao YX, Zhou ZM, Yang SW, Wang ZJ. Anatomical study of forearm arteries with ultrasound for percutaneous coronary procedures. *Circulation Journal*. 2010:1003020628-. Available from: https://doi.org/10.1253/circj.CJ-09-0577
40. Tomiyama Y, Yoshinaga K, Fujii S, Ochi N, Inoue M, Nishida M, Aziki K, Horie T, Katoh C, Tamaki N. Accurate quantitative measurements of brachial artery cross-sectional vascular area and vascular volume elastic modulus using automated oscillometric measurements: comparison with brachial artery ultrasound. *Hypertension Research*. 2015 Jul;38(7):478-84. Available from: https://doi.org/10.1038/hr.2015.6
41. Tayal R, Iftikhar H, LeSar B, Patel R, Tyagi N, Cohen M, Wasty N. CT angiography analysis of axillary artery diameter versus common femoral artery diameter: implications for axillary approach for transcatheter aortic valve replacement in patients with hostile aortoiliac segment and advanced lung disease. *International Journal of Vascular Medicine*. 2016 Mar 27;2016. Available from: https://doi.org/10.1155/2016/3610705
42. Tapia-Nañez M, Landeros-Garcia GA, Sada-Treviño MA, Pinales-Razo R, Quiroga-Garza A, Fernandez-Rodarte BA, Elizondo-Omaña RE, Guzman-Lopez S. Morphometry of the aortic arch and its branches. A computed tomography angiography-based study. *Folia Morphologica*. 2021;80(3):575-82. doi: 10.5603/FM.a2020.0098
43. Mehinovic A, Isakovic E, Delic J. Variations in diameters of vertebro-basilar tree in patients with or with no aneurysm. *Medical Archives*. 2014 Feb;68(1):27. doi: 10.5455/medarh.2014.68.27-29
44. Mujagic S, Moranjkic M, Mesanovic N, Osmanovic S. The inner diameter of arteries of the circle of Willis regarding gender and age on magnetic resonance angiography. *Acta Medica Saliniana*. 2013 Jul 1;42(2):6. doi: 10.5457/342
45. Nasr AY. The radial artery and its variations: anatomical study and clinical implications. *Folia Morphologica*. 2012;71(4):252-62. Available from: https://journals.viamedica.pl/folia_morphologica/article/view/19687
46. Singh M, Jaiswal S, Sharma PK, Vaidya VK. A Cadaveric Study of the Length of the Brachial Artery and its Clinical Correlation. *Era's Journal of Medical Research*. 2020;7(1):72-4. doi: 10.24041/ejmr2020.12
47. Majumdar S, Bhattacharya S, Chatterjee A, Dasgupta H, Bhattacharya K. A study on axillary artery and its branching pattern among the population of West Bengal, India. *Ital J Anat Embryol*. 2013:159-71. PMID: 25338405. Available from: https://pubmed.ncbi.nlm.nih.gov/25338405/

48. Poonam NJ, Singla RK, Sharma T. Anatomical considerations and clinical implications of subclavian artery. *J Evol Med Dental Sci*. 2013;2:5484-91.
49. Woraputtaporn W, Ananteerakul T, Iamsaard S, Namking M. Incidence of vertebral artery of aortic arch origin, its level of entry into transverse foramen, length, diameter and clinical significance. *Anatomical Science International*. 2019 Sep;94(4):275-9. Available from: https://doi.org/10.1007/s12565-019-00482-6
50. Gunnal SA, Farooqui MS, Wabale RN. Study of posterior cerebral artery in human cadaveric brain. *Anatomy Research International*. 2015;2015. doi: 10.1016/j.jasi.2016.08.171
51. Nader E, Skinner S, Romana M, Fort R, Lemonne N, Guillot N, Gauthier A, Antoine-Jonville S, Renoux C, Hardy-Dessources MD, Stauffer E. Blood rheology: key parameters, impact on blood flow, role in sickle cell disease and effects of exercise. *Frontiers in Physiology*. 2019 Oct 17;10:1329. Available from: https://doi.org/10.3389/fphys.2019.01329
52. Fitridge R, Thompson M. Vascular Arterial Haemodynamics. ln: editors. Mechanisms of Vascular Disease: *A Reference Book for Vascular Specialists. Adelaide (AU): University of Adelaide Press*; 2011. PMID: 30484990. Available from: https://www.ncbi.nlm.nih.gov/books/NBK534265/
53. Khalfin, Michael. fluid-dynamics-model. GitHub repository, 2021. Available from: https://github.com/michael-khalfin/fluid-dynamics-model
54. Bebry, A. Arterial Blood Velocities Consultation. [Personal interview, 5 Nov] (Unpublished).
55. Kuns B, Rosani A, Varghese D. Memantine. StatPearls [Internet]. 2021 Mar 13. PMID: 29763201. Available from: https://www.ncbi.nlm.nih.gov/books/NBK500025/
56. Kuns B, Rosani A, Varghese D. Donepezil. StatPearls [Internet]. 2021 Mar 13. PMID: 29763201. Available from: https://www.ncbi.nlm.nih.gov/books/NBK500025/
57. Arnol'd VI. Instability of dynamical systems with several degrees of freedom. InHamiltonian Dynamical Systems 2020 Aug 17 (pp. 633-637). CRC Press.
58. Kovacs GG. Chapter 25 - Tauopathies. Handbook of Clinical Neurology. 2018 Jan 1;145:355-68. Available from: https://doi.org/10.1016/B978-0-12-802395-2.00025-0
59. Patel MP, Patel RR, Patel JK. Chitosan mediated targeted drug delivery system: a review. Journal of pharmacy & pharmaceutical sciences. 2010 Nov 16;13(4):536-57. Available from: https://doi.org/10.18433/J3JC7C
60. Hurtado DE, Molina-Porcel L, Iba M, Aboagye AK, Paul SM, Trojanowski JQ, Lee VM. Aβ accelerates the spatiotemporal progression of tau pathology and augments tau amyloidosis in an Alzheimer mouse model. The American Journal of Pathology. 2010 Oct 1;177(4):1977-88. Available from: https://doi.org/10.2353/ajpath.2010.100346

61. Leroy K, Ando K, Laporte V, Dedecker R, Suain V, Authelet M, Héraud C, Pierrot N, Yilmaz Z, Octave JN, Brion JP. Lack of tau proteins rescues neuronal cell death and decreases amyloidogenic processing of APP in APP/PS1 mice. *The American Journal of Pathology*. 2012 Dec 1;181(6):1928-40. Available from: https://doi.org/10.1016/j.ajpath.2012.08.012
62. Goodman M. Future crimes: Everything is connected, everyone is vulnerable and what we can do about it. Anchor; 2015 Feb 24. Available from: https://books.google.com/books?hl=en&lr=&id=5v99BAAAQBAJ&oi=fnd&pg=PT9&dq=can+nanotechnology+be+hacked&ots=2KZ3Fzo24-&sig=NsYEdXxgwo1ydYEsfSO3IhRy0wQ#v=onepage&q=can%20nanotechnology%20be%20hacked&f=false
63. Simpson, S. Encryption. The University of Texas at Austin. 1997. Available from: https://www.laits.utexas.edu/~anorman/BUS.FOR/course.mat/SSim/history.html
64. Zhou X, Tang X. Research and implementation of RSA algorithm for encryption and decryption. InProceedings of 2011 6th international forum on strategic technology 2011 Aug 22 (Vol. 2, pp. 1118-1121). IEEE. Available from: https://ieeexplore.ieee.org/abstract/document/6021216
65. Stinson DR. Cryptography: theory and practice. Chapman and Hall/CRC; 2005 Nov 1. Available from: https://api.taylorfrancis.com/content/books/mono/download?identifierName=doi&identifierValue=10.1201/9781420057133&type=googlepdf

Bibliography

1. Korolev IO. Alzheimer’s disease: a clinical and basic science review. Medical Student Research Journal. 2014 Sep;4(1):24-33.
2. Braak H, Braak EV. Staging of Alzheimer's disease-related neurofibrillary changes. Neurobiology of aging. 1995 May 1;16(3):271-8.
3. Colin M, Dujardin S, Schraen-Maschke S, Meno-Tetang G, Duyckaerts C, Courade JP, Buee L. From the prion-like propagation hypothesis to therapeutic strategies of anti-tau immunotherapy. Acta neuropathologica. 2020 Jan;139(1):3-25.
4. Watts DJ, Strogatz SH. Collective dynamics of ‘small-world’ networks. nature. 1998 Jun;393(6684):440-2.
5. Ahmad J, Akhter S, Rizwanullah M, Ahmed Khan M, Pigeon L, T Addo R, H Greig N, Midoux P, Pichon C, Amjad Kamal M. Nanotechnology based Theranostic approaches in Alzheimer's disease management: current status and future perspective. Current Alzheimer Research. 2017 Nov 1;14(11):1164-81.
6. Secomb TW. Hemodynamics. Comprehensive physiology. 2016;6(2):975.

7. Jambhekar SS, Breen PJ. Basic pharmacokinetics. London: Pharmaceutical Press; 2009.
8. Aminzadeh F, Byszewski A, Molnar FJ, Eisner M. Emotional impact of dementia diagnosis: exploring persons with dementia and caregivers' perspectives. Aging and Mental Health. 2007 May 1;11(3):281-90.
9. *Khan Academy*. Accessed January 24, 2017. Available from: https://www.khanacademy.org.